



**HAL**  
open science

# Investigation of hydrodynamic cavitation induced reactive oxygen species production in microchannels via chemiluminescent luminol oxidation reactions

Darjan Podbevšek, Gilles Ledoux, Matevž Dular

## ► To cite this version:

Darjan Podbevšek, Gilles Ledoux, Matevž Dular. Investigation of hydrodynamic cavitation induced reactive oxygen species production in microchannels via chemiluminescent luminol oxidation reactions. *Water Research*, 2022, 220, pp.118628. 10.1016/j.watres.2022.118628 . hal-03681503

**HAL Id: hal-03681503**

**<https://hal.science/hal-03681503>**

Submitted on 30 May 2022

**HAL** is a multi-disciplinary open access archive for the deposit and dissemination of scientific research documents, whether they are published or not. The documents may come from teaching and research institutions in France or abroad, or from public or private research centers.

L'archive ouverte pluridisciplinaire **HAL**, est destinée au dépôt et à la diffusion de documents scientifiques de niveau recherche, publiés ou non, émanant des établissements d'enseignement et de recherche français ou étrangers, des laboratoires publics ou privés.



# Investigation of hydrodynamic cavitation induced reactive oxygen species production in microchannels via chemiluminescent luminol oxidation reactions

Darjan Podbevšek<sup>a,\*</sup>, Gilles Ledoux<sup>b</sup>, Matevž Dular<sup>a</sup>

<sup>a</sup> Faculty of Mechanical Engineering, University of Ljubljana, Askerčeva 6, 1000 Ljubljana, Slovenia

<sup>b</sup> Institut Lumière Matière, Université Claude Bernard Lyon 1, 69622 Villeurbanne, France

## ARTICLE INFO

### Keywords:

Cavitation cloud shedding  
Free radicals  
Photon counting  
Microscale cavitation  
Luminol chemiluminescence  
Convergent-divergent channels

## ABSTRACT

Hydrodynamic cavitation was evaluated for its reactive oxygen species production in several convergent-divergent microchannel at the transition from micro to milli scale. Channel widths and heights were systematically varied to study the influence of geometrical parameters at the transitory scale. A photomultiplier tube was used for time-resolved photon detection and monitoring of the chemiluminescent luminol oxidation reactions, allowing for a contactless and *in situ* quantization of reactive oxygen species production in the channels. The radical production rates at various flow parameters were evaluated, showing an optimal yield per flow rate exists in the observed geometrical range. While cavitation cloud shedding was the prevailing regime in this type of channels, the photon arrival time analysis allowed for an investigation of the cavitation structure dynamics and their contribution to the chemical yield, revealing that radical production is not linked to the synchronous cavitation cloud collapse events. Instead, individual bubble collapses occurring throughout the cloud formation were recognized to be the source of the reactive oxygen species.

## 1. Introduction

The liquid to vapor phase transition, known as cavitation, occurs as a pressure decrease in the liquid drives the vapor bubble growth and subsequent collapse, as the pressure normalizes. This can occur in liquids that are subjected to acoustic excitation (ultrasonic cavitation - UC) or in hydrodynamic systems, where a constriction in the flow causes a low-pressure region to form due to Bernoulli's principle (hydrodynamic cavitation - HC). It is an established principle in cavitation bubble dynamics, that the compression of the content during the rapid bubble collapse leads to high temperatures and pressures inside the bubble, which can lead to plasma formation, luminescence and exotic chemical species production, including free radical and other highly reactive species (Suslick, 1997). These species form due to the extreme thermodynamic conditions during peak collapse, where homolytic splitting of water takes place and are thought to be critical in cavitation-based advanced oxidizing processes (Wood et al., 2017), such as material functionalization (Guittonneau et al., 2010), fuel desulfurization (Cako et al., 2022) and waste-water treatment (Gagol et al., 2018; Lalwani et al., 2020; Zupanc et al., 2019). The latter is often coupled with other

advanced oxidation processes to achieve synergetic effects, which can reduce the cost of such processes and make its use more feasible (Fedorov et al., 2022; Gagol et al., 2020), however such treatment can be accompanied with unwanted nitration side reactions with toxic products that should be mitigated when the mineralization process is not complete (Rayaroth et al., 2022).

The chemical effects of cavitation are well known in UC (Suslick, 1989), but have only in recent years started to be explored for HC (Gagol et al., 2018). Generally, UC and HC have very different bubble dynamics, as the former is based on periodic excitation, while the latter is excited by a single low-pressure pulse. Scaling down from macro to micro scale is expected to produce a more efficient bubble collapse, as smaller bubble sizes should, due to higher Laplace pressure, lead to better sphericity retention during the collapse phase, as it can better resist the deformation due to pressure gradients in the flow and should therefore reach higher thermodynamic extremes in the bubble core at peak bubble collapse. Furthermore, the bubble growth timescale at around 20 $\mu$ s can approach the single period of low frequency ultrasonic cavitation, as was found in a recent study (Podbevšek et al., 2021a). Hydrodynamic cavitation at the microscale is only beginning to be

\* Corresponding author.

E-mail address: [darjan.podbevsek@gmail.com](mailto:darjan.podbevsek@gmail.com) (D. Podbevšek).

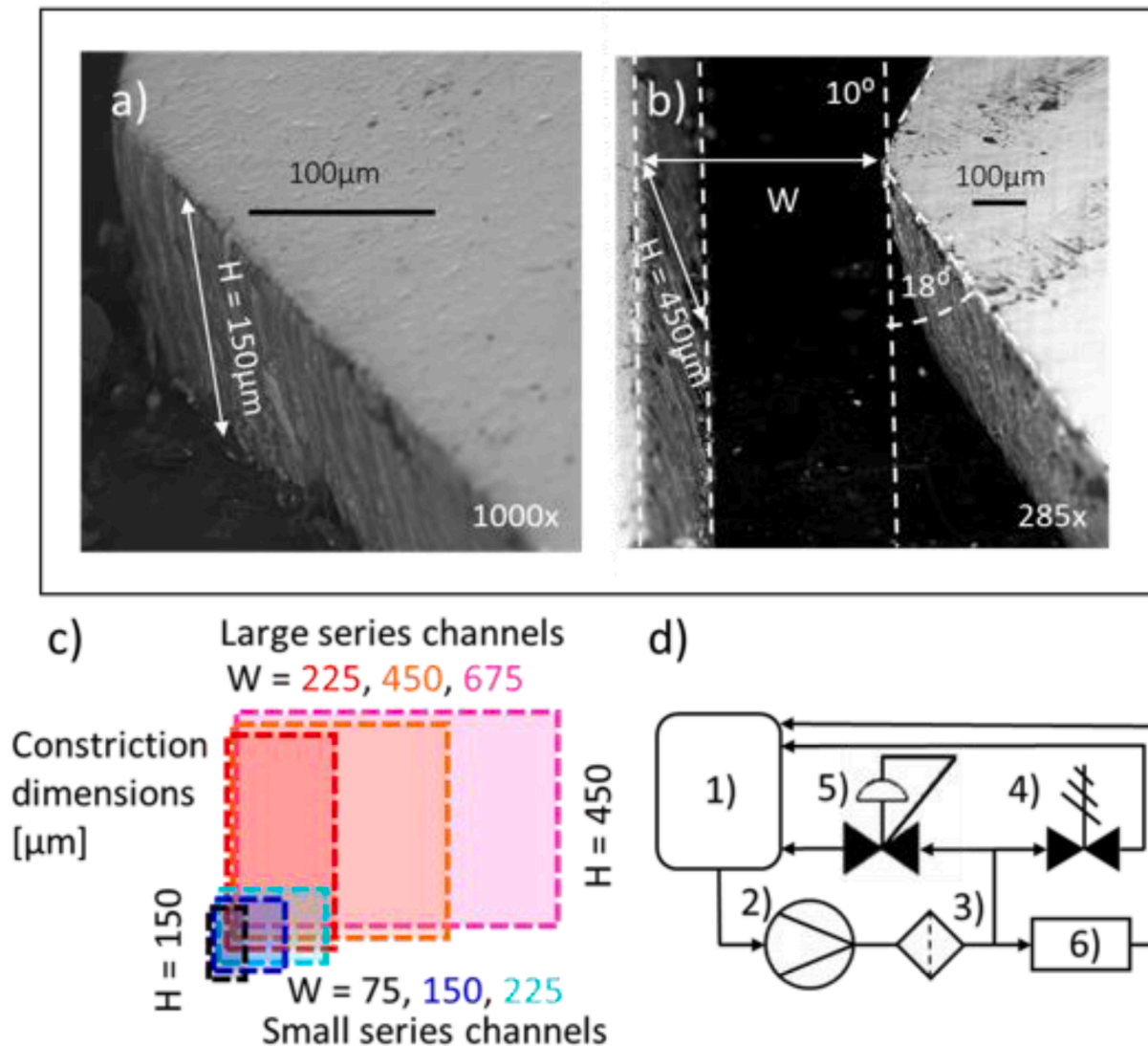


**Fig. 1.** a) electron microscope image of the channel inner wall roughness for the  $H = 150\mu\text{m}$  channel series. b) the channel geometry shown on a electron microscope image for the  $H = 450\mu\text{m}$  channel series. channel downstream area is in towards the  $10^\circ$  channel slope. c) different constrictions dimensions studied. The colour scheme for each constriction is kept constant throughout the article. d) The schematic of the experimental liquid line: reservoir (1), micropump (2),  $1\mu\text{m}$  filter (3), pressure relief valve (4), back pressure regulator with manometer (5), microchannel assembly (6)

explored and offers a fundamental view into the HC phenomenon. Moreover, microfluidic systems enable us to minimize the quantity of the liquids used, crucial when studying minute quantities of toxic or exotic liquids, as well as offering easy coupling with optical probing techniques (Ayela et al., 2013; Kim et al., 2017). In such systems, the liquids flowing through micro-scale constrictions often have to be filtered to prevent clogging, which can also remove the nuclei from the liquids, allowing for liquid metastability, often manifested as the delay in cavitation inception. Despite the advantages, only a few groups use microfluidics to study the cavitation phenomenon (Aghdam et al., 2019; Ayela et al., 2017, 2013; Cole et al., 2006; Gevari et al., 2019; Ghorbani, 2021; Ghorbani et al., 2018b, 2018c, 2018a, 2017b, 2017a; Gothsch et al., 2015; Hosseinpour Shafaghi et al., 2021; Medrano et al., 2012, 2011; Mishra and Peles, 2006, 2005a, 2005b; Mishra and Peles, 2006, 2005; Mishra and Peles, 2004; Mossaz et al., 2017; Nayebzadeh et al., 2018; Peles and Schneider, 2006; Perrin et al., 2021; Podbevšek et al., 2018; Podbevšek et al., 2021a, 2021b; Qiu et al., 2019, 2017; Rokhsar Talabazar et al., 2021; Rooze et al., 2012; Schneider et al., 2007; Singh and Peles, 2009; Stieger et al., 2017). Cavitation cloud shedding is a typical and dominating event occurring in hydrodynamic cavitation, often observed in convergent-divergent and venturi channels at the

macroscale. Typically, these cavitation cloud structures grow until they shed off in a periodic manner, usually with well-defined shedding frequencies. This can lead to a powerful and coordinated collapse of the main vapor cloud structure and the rest of the vapor bubbles in the channel, due to the shockwave triggered by the main cloud collapse. This simultaneous energetic event has been known to induce erosion, noise, and other phenomena in hydrodynamic cavitating flow (Dular et al., 2006).

There are several studies, focusing on cavitation based radical production and waste-water treatment, usually aimed at specific pollutants, typically requiring the analysis of the degradation product or trapping agents. Observing the degradation of p-nitrol (Kalumuck and Chahine, 2000), Rhodamine B (Mishra and Gogate, 2010; Wang et al., 2009), BTEX (benzene, toluene, ethylbenzene, xylene) (Braeutigam et al., 2009; Fedorov et al., 2021, 2020), benzene to phenol (Batoveva et al., 2011) and the Weissler reaction (tri-iodide oxidation) (Gogate et al., 2001) were all used to assess the oxidative potential of HC. The latter was later shown to degrade even without the presence of cavitation, possibly due to temperature increase or copper induces surface catalytic reactions (Morison and Hutchinson, 2009). Terephthalic (Gielen et al., 2016) and salicylic acid dosimetry (Arrojo et al., 2007; Arrojo and Benito, 2008) is

also used for hydroxyl radical specific analysis, but the latter has recently been shown to influence the surface tension in the liquid and thus effecting cavitation bubble dynamics (Zupanc et al., 2020), so care must be taken in the interpretation of the results. However, the chemiluminescent (CL) reactions of luminol with radical species has been used to study radical production from ultrasonic (Fernandez Rivas et al., 2012; Hatanaka et al., 2002; McMurray and Wilson, 1999; Price et al., 2010; Renaudin et al., 1994; Rooze et al., 2013; Son et al., 2020; Yin et al., 2014) and hydrodynamic cavitation (Perrin et al., 2021; Podbevšek et al., 2018; Podbevšek et al., 2021a; Schlender et al., 2016). Recently, an *in situ*, quantitative method, based on single photon counting of luminol chemiluminescent reactions has been developed (Podbevšek et al., 2018; Podbevšek et al., 2021a), which dramatically decreases the analysis time, as the radical production is obtained from the detected photons, without the need for time consuming sampling and chemical analysis. The technique allows us to study *in situ* production of radicals in the channel in a non-invasive manner. This is important, as the two-phase hydrodynamic flows tend to be very sensitive to perturbations, especially at the microscale.

In this article we study the scaling effect on primary hydroxyl radical production, along with secondary recombinant reactive oxygen species (ROS) with potential to oxidize luminol (hereafter referred to as ROS), in micro to mill scale convergent-divergent channels, by quantifying luminol chemiluminescent reactions through single photon counting. The ROS yield was examined for different flow parameters in each of the six microchannels of varying geometries. The cavitation cloud shedding event, a typical periodic cavitation structure growth and collapse is present in most of the 0 - 10bar driving pressure range examined in this study. By monitoring the photon arrival times and the vaporous structure dynamics, we can uncover the relevant mechanism for radical production in microscale hydrodynamic cavitation reactors.

## 2. Material and methods

### 2.1. Microfluidic channel geometry and flow parameters

A series of microchannels were laser cut from 150 and 450  $\mu\text{m}$  thick AISI 316L stainless-steel sheets, which determines the height (H) of the channel. One side of the geometry is straight while the other forms a convergent-divergent ( $18^\circ/10^\circ$ ) slope of the micro channel, as seen on the electron microscope image of the constriction on Fig. 1a, b, for the small and the large channel series, respectively. A symmetric channel design, with both sides angled was initially considered, however, such channels showed various different cavitation regimes at a particular driving pressure (similar to observations in certain micro-diaphragms used in (Podbevšek et al., 2018; Podbevšek et al., 2021a)), which tend to stochastically interchange during measurement. This design was eventually abandoned, as it proved difficult to work with due to unstable flow conditions. Three constriction widths (W) 0.5H, H and 1.5H for each channel height group, with about 27mm from constriction to the end of the divergent part of channel. The plate was placed between two acrylic glass plates, together forming the microchannel assembly, like the setup used in (Podbevšek et al., 2021b). When observing cavitation at the microscale, a delay in cavitation inception is often observed, due to the liquid metastability caused by the lack of nucleation sites (Medrano et al., 2011; Podbevšek et al., 2018). For our channels, the smaller 150 $\mu\text{m}$  heights channel group (small series channels), metastable flow could be easily observed, while in the 450 $\mu\text{m}$  height channels (large series channels), the metastability was more subtle. As nucleation is a stochastic process, there is a certain probability that the liquid will cavitate at a given driving pressure ( $p_{\text{cav}}$ ). The  $p_{\text{cav}}$  was measured for each channel, by increasing the pressure in 0,1bar increments and allowing 10s for metastable flow to jump to cavitating flow, if thermodynamically favorable. This was averaged over 10 rounds, with the standard deviation and measurement uncertainty amounting to less than 0.1bar, for most channels. The different dimensionless numbers used in

the study are the hydraulic diameter:  $D_h = 4A / \Gamma$ , where  $\Gamma$  is the perimeter of the channel constriction and A the cross-sectional area; the Reynolds number -  $Re = v * D_h / \nu$ ,  $\nu$  being the velocity at the constriction and  $\nu$  the kinematic viscosity; and the Cavitation number -  $\sigma = 2(p - p_v) / \rho * v^2$ , with  $\rho$  the liquid density,  $p$  and  $p_v$  the upstream and saturation vapor pressure at outlet conditions (20°C and 1atm), respectively. All values marked with the “<sub>cav</sub>” subscript are calculated from the measured  $p_{\text{cav}}$  value, representing the value at cavitation inception ( $Q_{\text{cav}}$ ,  $v_{\text{cav}}$ ,  $\sigma_{\text{cav}}$ ,  $Re_{\text{cav}}$ ). For the  $\sigma_{\text{cav}}$ , the velocity at the constriction is the cavitation inception velocity -  $v_{\text{cav}}$ .

### 2.2. Liquid line and luminol solution

The liquid line of the experiment is shown in Fig. 1d. The working liquid was a 1mM aqueous solution of 3-aminophthalhydrazide 97% (luminol) from Sigma-Aldrich in 3.75mM NaOH (11.4pH), which was placed in a borosilicate glass bottle (1), serving as the liquid reservoir. A small gear pump (2) propelled the liquid through a 1” diameter 1 $\mu\text{m}$  glass fiber filter and a 10 $\mu\text{m}$  nylon mesh (3). The safety valve (4) was present to prevent over-pressurization of the system, while a back-pressure regulator controlled (5) the upstream pressure in the channel (6). The constriction in the micro channel presented the smallest cross-section and therefore the main resistance to the flow. Meanwhile, the downstream pressure was equal to 1atm, as the liquid from (4, 5 and 6) was collected in the open reservoir. The pressure difference across the constriction (driving pressure) is therefore, the difference between the set upstream and the downstream pressure. The temperature of the liquid was monitored by a K-type thermocouple and did not rise by more than 1°C during the experiments. The mass flows at specific driving pressures were determined by a digital scale, averaged at least over 10s, for each upstream pressure condition.

### 2.3. Optical setup and radical detection

The photon yield was acquired with an optical setup similar to previous publications (Podbevšek et al., 2018; Podbevšek et al., 2021a). A R9789 photomultiplier tube (PMT) from EMI, was placed downstream of the constriction, covering most of the downstream area of the channel, to measure the CL emission. An ORTEC 935Quad preamplifier and ORTEC 935Quad CFD discriminator were used for pre-treatment of pulses created by the PMT, with the NI USB-6003 DAQ counter used to acquire the final photon flux, with the temporal resolution for the photon arrival times roughly 1 $\mu\text{s}$ . The  $\frac{1}{2}$ ” PMT detector was 35mm from the cavitation region, with the chemiluminescence passing through 10mm of plexiglass, with the transmission coefficient of 0.66 at the luminol peak emission wavelength. Other coefficients were considered when determining the ROS from the detected photons: a) the solid collection angle through the plexiglass to the PMT detector was 0.0552sr making the collection coefficient 0.0044, b) the chemiluminescent reaction quantum yield at 0.0124 (Lee and Seliger, 1972) and c) PMT quantum yield for the luminol emission spectrum (425nm peak) at 0.15042 (Podbevšek et al., 2018; Podbevšek et al., 2021a). Therefore, with our current optical setup, each photon detected corresponds to  $\sim 1.85 * 10^5$  oxidation reactions taking place in the channel, due to the ROS formed by the hydrodynamic cavitation. Averaging the photon count per second can therefore be expressed as a number of species detected in attomoles per second (amol/s) - the chemical yield. Single photon detection requires black-out conditions, to allow for the detection of the weak CL signal. The photon yields measurements were averaged over 60s, with background and sonoluminescent signals (if present) subtracted.

The fast camera recording was taken with a Photron Fastcam SA-Z 2100K-M-64GB and the AS-F VR Micro-Nikkor 105mm camera objective, at 100000FPS, in 0.05s clips and a 250ns shutter speed, with backlight illumination provided by a LED through a diffusion plate at the back side of the transparent plexiglass microchannel wall. The average

**Table 1**

Microchannel geometry and flow parameters. The channel name: S = small and L = large series channels for the first letter, while the second letter indicates the aspect ratio of W:H (A = 0.5, B = 1, C = 1.5).

Channel name	Channel height – H [μm]	Channel width at constriction – W [μm]	Constriction cross-section [μm <sup>2</sup> ]	D <sub>h</sub> [μm]	Q <sub>cav</sub> [g/s]	p <sub>cav</sub> [bar]	σ <sub>cav</sub> [-]	V <sub>cav</sub> [m/s]	Re <sub>cav</sub> [-]
SA	150 (small channel series)	75	11250	100	0.364	2.1	0.188	32.45	3080
SB		150	22500	150	0.945	4.05	0.122	42.12	5998
SC		225	33750	180	0.965	3.26	0.241	28.68	4901
LA	450 (large channel series)	225	101250	300	2.23	0.87	0.373	22.09	6291
LB		450	202500	450	4.01	0.98	0.503	19.86	8484
LC		675	303750	540	6.53	1.71	0.427	21.56	11053

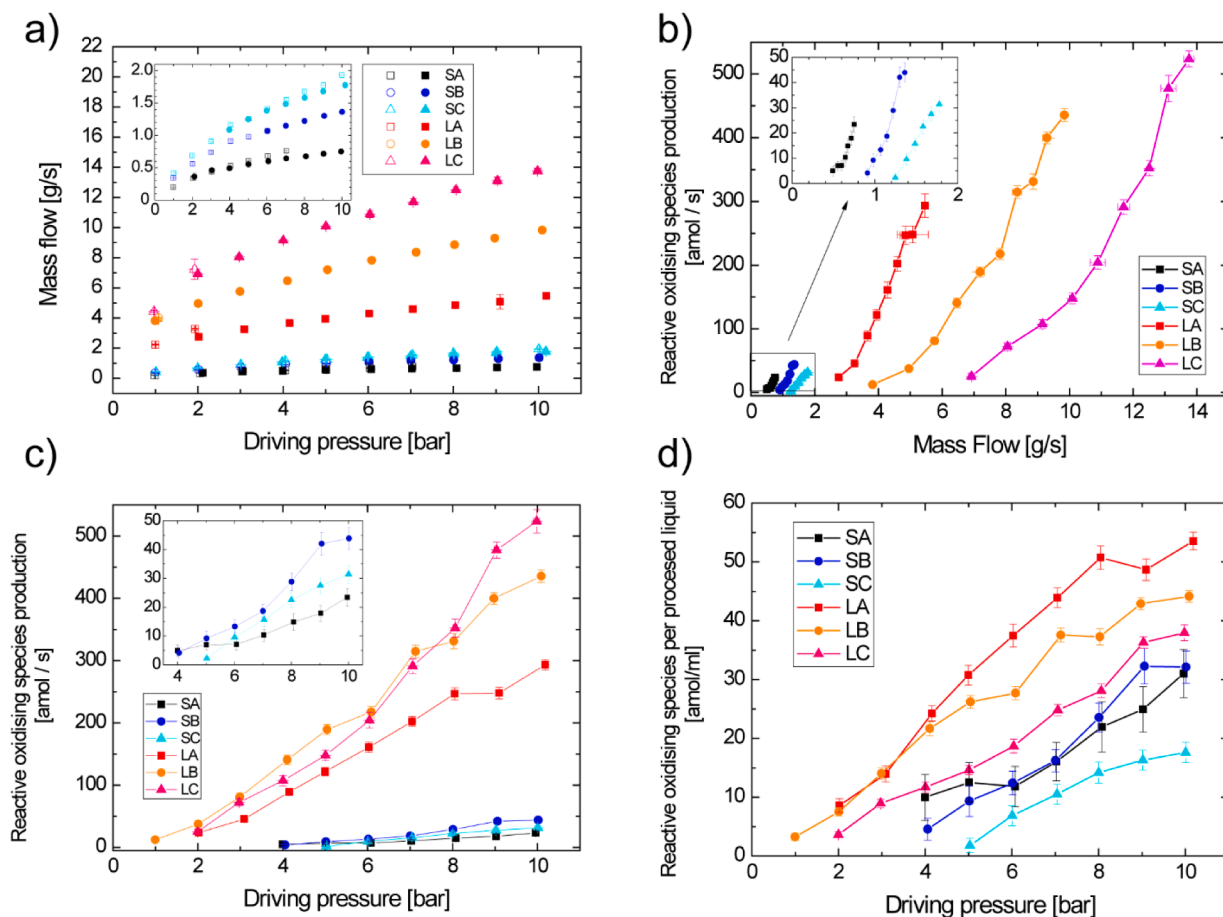


**Fig. 2.** Flow parameters and the reactive oxygen species (ROS) production for the six channels studied. a) Mass flow at driving pressure, with a close up for the small channel series. The empty and filled symbols represent the single and the two-phase flow respectively. b) ROS production per second (amol/s) in relation to the mass flow through the constriction. c) ROS production per second in relation to the driving (upstream) pressure through the constriction. d) ROS production per treated volume of liquid (amol/ml) at different driving pressures.

cloud length was determined by analyzing the standard deviation of the recorded series over several cloud shedding events, as used in previous cavitation dynamics studies (Dular et al., 2004).

### 3. Results

#### 3.1. Flow characterization and radical yield

The channels geometries selected for these studies range from micro to near-millimeter scale. Channel constriction dimensions (W to H ratio) are indicated in Table 1, along with the channel naming protocol in the caption. We can see the smaller series channels present different cavitation parameters, mostly stemming from higher p<sub>cav</sub> values. The transition to cavitating flow at the microscale is known to be metastable for pure liquids (Medrano et al., 2012, 2011; Peles, 2008; Podbevšek et al.,

2018). We can observe metastability before cavitation inception in all three small channel series, but the effect is lesser or non-existent with the large series channels. This can be seen in Fig. 2a, where we see the mass flow vs driving pressure relationship of all the channels examined. There is an overlapping region of single and two-phase flow for the small series channels, where the liquid exhibits metastability due to the removal of the nucleation sites and the smooth walls of the microchannels, as mentioned in the experimental setup section. The rest of Fig. 2 addresses the relationship to the radical production in the channels at different flow conditions. In Fig. 2b and c, we see the reactive oxygen species yield (amol/s) at different mass flow and driving pressure through the constriction, respectively. Generally, there is a trend of rising radical production with increasing constriction cross-section, the exception being the SC channel, which shows radical below that of SB. On the other hand, Fig. 2d shows the radical production per processed

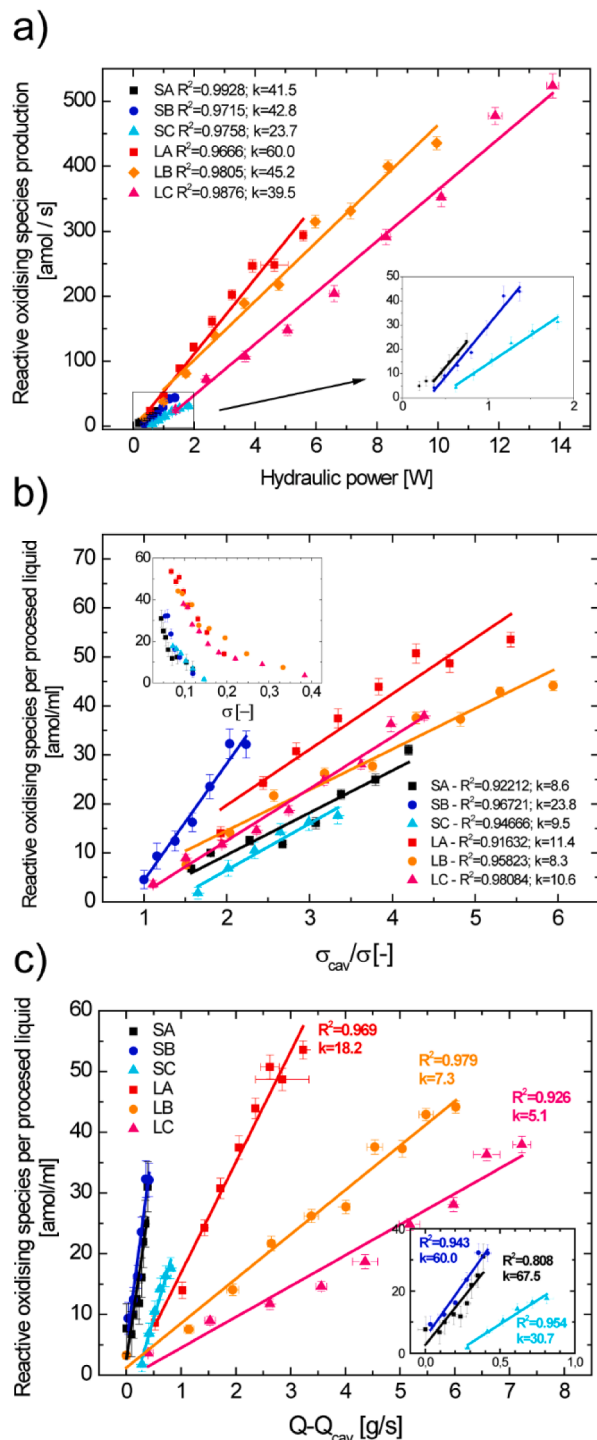


**Fig. 3.** a) ROS production (amol/s) in individual channels as a function of the hydraulic power in the flow. The smaller window is a close up of the small series channels. b) ROS production per processed volume of liquid (amol/ml), as a function of the dimensionless  $\sigma_{cav}/\sigma$  parameter. The auxiliary window shows the ROS/ml for the  $\sigma$  parameter (data in supplemental file 1). c) ROS production per processed volume of liquid, as a function of the dimensionless  $Q-Q_{cav}$  parameter. The smaller window is a close up of the small series channels.

liquid volume (amol/ml) at different driving pressure; when considering this parameter, it is immediately obvious that the biggest channels are not necessarily optimal for radical production, as was the case for the ROS yield. For the large series channels, the inverse relationship is true, as the LA channel outperforms the wider LB, and both outperform the

widest LC channel. Moreover, the latter (LC) shows only slightly higher amol/ml values than the smallest ones (SA and SB), whose rates overlap throughout most of the pressure range. The LA and LB channels show uniform production at low driving pressure, which only starts diverging above 4bar. Overall, we can see that the two widest channels (1.5 aspect ratio) in both large and small channel groups show the weakest radical yield per processed liquid volume for the particular group (SC, LC).

Fig. 3 shows the radical production with different flow parameters and dimensionless cavitation intensity markers. Linear progressions are shown, similar to previous studies on smaller micro diaphragm type channels (Podbevšek et al., 2021a). The first graph shows the radical yield as a function of hydraulic power of the flow through the constriction. Most channels follow a similar slope with increasing driving pressure, with slightly higher k-values shown for LA and slightly lower for SC channel. Furthermore, the SA and SB slopes seem to overlap particularly well above 0.25W hydraulic power values. On Fig. 3b the auxiliary graph shows the radical yield per processed liquid volume as a function of the dimensionless cavitation number  $\sigma$ ; a value often used to characterize cavitation intensity. As it decreases, indicating increased cavitation activity, we see a gradual increase of the ROS yield per treated liquid volume. Two distinct group are formed, one for the small and one for the large series channels. For the  $\sigma$  normalized to the channels  $\sigma_{cav}/\sigma$ , we see a uniform, roughly linear trend between all channels, with the slope ranging from 8.3 to 11.4 amol/ml, with the exception of SB equaling to roughly double the value. The chemical yield at different  $Q-Q_{cav}$  values is presented in Fig. 3c, where we observe the smaller SA and SB channels production overlapping, whereas values for the rest of the channels vary. Here the tendency for the higher metastability of the smaller channel series seem to dominate over the high radical yield of the large channel group, as the decreasing k-values with increasing channel size seem to indicate. The linear trends observed for the radical production (amol/s and amol/ml) for different flow parameters, indicates a common mechanism is at play for all the channels in the study. To explain this, we examined the cavitation structures formed in the channels and their dynamics.

### 3.2. Cavitation structure dynamics and photon arrival times analysis

Fig. 4 and Fig. 5 show the typical cloud shedding event in the small and large channel series, respectively. The process usually starts with the attached cavity forming just downstream of the constriction. A vaporous void at the constriction eventually starts to shed individual cavitation bubbles, forming a “cavitation stream”, as best seen on Fig. 4. This stream grows further down the divergent part of the micro-venturi channel, until the flow recirculates, forming a vortex filled with cavitation bubbles. This is the beginning of the cavitation cloud, which will grow downstream and eventually shed off; at that point the cavitation stream will retreat upstream towards the constriction, restarting the process, while shed cloud collapses independently. Generally, the dominant feature of hydrodynamic cavitation at this scale is the relatively long-lived cloud shedding event, while the less obvious cavitation stream itself is composed of many individual bubble collapses, at much shorter timescales. Fig. 4 shows a typical cloud shedding event in the smaller series channels, where Kelvin-Helmholtz instabilities can appear on the vapor cavity near the constriction, as was recently reported in (Podbevšek et al., 2021b), and were shown to be linked to the cloud shedding event at the microscale. Cloud shedding event typical for large scale channels group is shown in Fig. 5, where the vaporous cavity at the mouth of the channel is seen more clearly. The cavity can momentarily disappear (at 2.5ms) and reform (at 3ms). A much more distinct and unified vaporous structure, surrounded by a small cavitation bubble stream appears, compared to the cavitation cloud in the small series channels, which is composed only of small bubbles. When the cavitation cloud reaches the end of the divergent part of the channel, the cavity collapses and the cavitation stream starts retreating downstream the constriction, as the cloud sheds off (5.85ms). The cloud collapse ensues

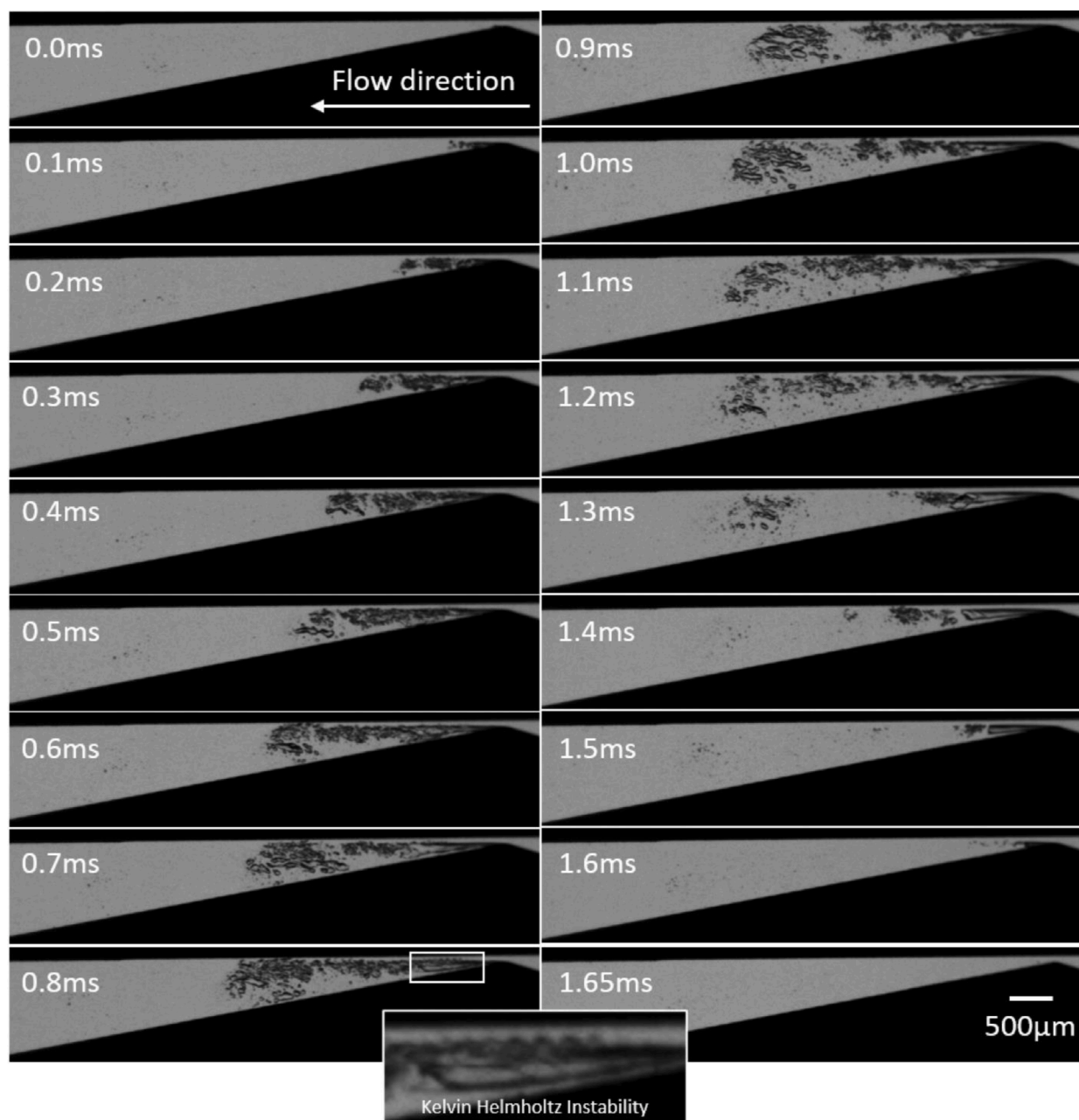


**Fig. 4.** Typical cavitation cloud shedding event in the small series channels. the figure shows the SA channel at 8bar. Kelvin-Helmholtz instabilities are also observed during the shedding event. The flow direction is flow right to left.

after the process restarts and a new cloud starts to grow (6.5 to 7.25ms). During most of the cloud shedding event, the small bubbles making up the cavitation stream, continuously grow and collapse in the cavitation stream throughout the channel. The cavitation stream mechanism seems to diminish or momentarily disappears only during the retreating phase, as the cloud sheds.

A time resolved analysis of the photon arrival times was also performed, shown on Fig. 6, with the red marks indicating individual photon arrival events. On the same figure we see the normalized average pixel value of an area near the constriction, where the black area is indicative of the cavitation stream disappearing from the channel. The periodic cloud shedding is captured this way, as the background (white = 1) pixel value is acquired only when the cavitation stream retreats back to the constriction, indicating no cavitation bubbles were present. The two separate, non-synchronized recordings show typical periodical behavior in the LB channel at 8bar driving pressure for the

chemiluminescent signal and cavitation shedding. This relationship is not always so distinctly visible for all channels and flow conditions, as an inherently low radical production might not produce a sufficient number of reactions (photons) to make the gap in the flow visible on the radical production timeline. This could be described as chemiluminescence under-sampling, and effects mostly the smaller channel group in our study. However, notably the observed photons are not observed in bursts corresponding to the cavitation cloud shedding frequencies, nor do they show an exponential decay trend, which might be expected from instantaneous energetic collapse events forming large amounts of ROS. In fact, the radical production is often seen increasing up until the cloud separation phase. It is clear the radicals are being produced throughout the cavitation cloud growth, not being confined to the cavitation cloud collapse event. Moreover, the average period 8.8ms ( $\pm 1.99$ ms) and the average gap time of 3.04ms ( $\pm 0.64$ ms) for the photon arrival times is in agreement to the gap 2,5ms ( $\pm 0.68$ ms) and

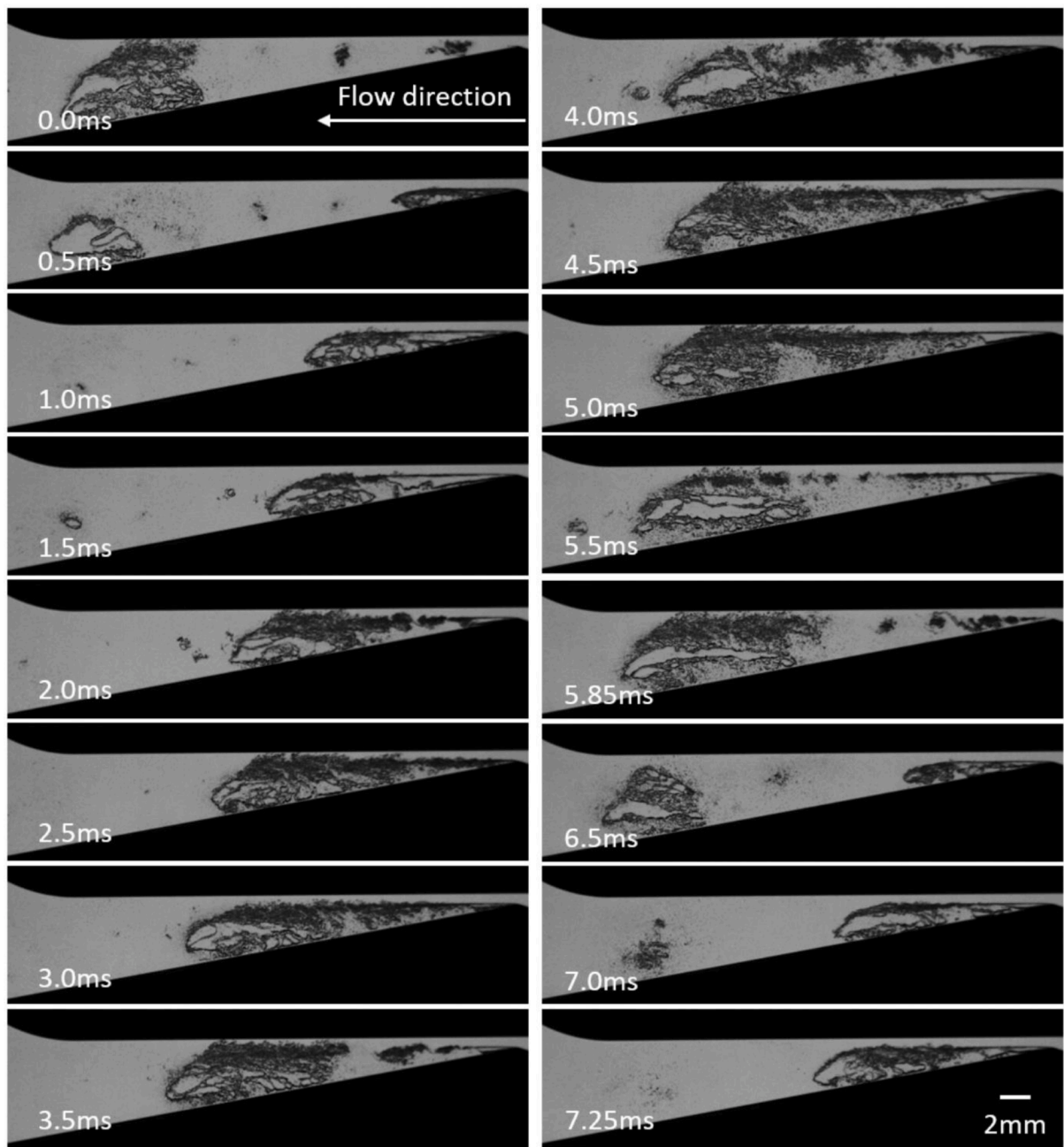


Fig. 5. Typical cavitation cloud shedding event in large series channels (LC channel at 10bar driving pressure). The flow direction is flow right to left.

the period  $9.17 (\pm 1.06\text{ms})$  found from the image analysis, indicating that when the cavitation stream retreats, the radical production in the flow stops.

A more careful examination of the cloud shedding frequency in the different channel geometries can be found in Fig. 7. The full symbols represent full cavitation cloud shedding mechanism, while the empty symbols are the regimes where developed cavitation is present with partial or transitory cloud shedding. All the channels show faster cloud shedding at lower Re numbers (lower driving pressure). These typically level off for the large channel series, while they continually drop for the smaller channels. The small channel group tends to form distinctive cavitation clouds when the frequency approaches 600Hz, while for the large channel group the frequency is around 300Hz. Channel SC shows the transition at 9 bar (780Hz) and is fully shedding at 10bar (610Hz), while for the SB and SA channels the transition is at 7 (640Hz) and 8 bar (620Hz) respectively. The larger series channels all show partial

shedding at 2 bar with frequencies between 360 to 500Hz and fully shedding at 3bar with frequencies around 300Hz. However, no distinct discontinuities in the radical production rates are observed for any of the channels at the values where the cloud shedding frequencies change abruptly, which might indicate that the increased cloud shedding frequencies would be producing more oxidation events. In fact, no obvious correlation is observed between the rate of cloud collapse events, which are increased at lower driving pressures and the ROS ( $\text{amol/s}$  or  $\text{amol/ml}$ ) yields, which increase with increasing driving pressure.

For the channels used in our study, only the height and the width of the channel are varied, while the rest of the geometry is uniform for all channels. In the small series channels, the cloud shedding event is taking place entirely within the divergent part of the micro venturi. However, for the large channel series, the shed clouds can leave the divergent region of the channel at higher driving pressure. In Fig. 8, the standard deviation analysis of the recorded series, shows the downstream cloud

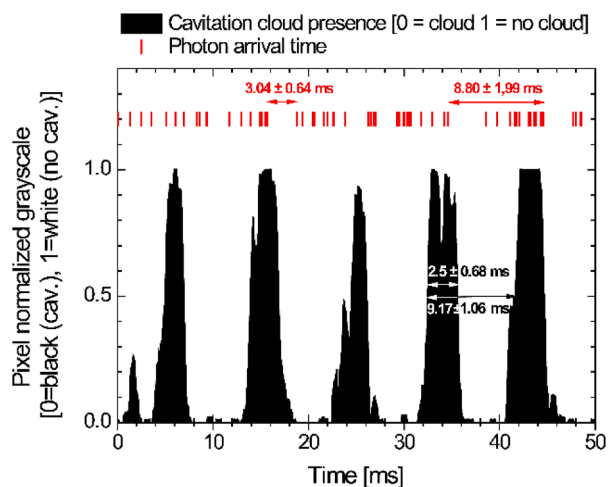


**Fig. 6.** The photon arrival times (red marks) indicating chemiluminescent oxidation of luminol by reactive oxygen species in the flow compared to the cloud shedding events timeline. The data sets are from two separate (non-synchronised) experiments and represent the typical behaviour in the LB channel at 8bar driving pressure. The average gap and average period times of the two data sets are indicated in the graph. The shedding events gap and period corresponding to no/low cavitation activity, gathered from the high-speed recording, seems to correspond to the gaps and the period on photon arrival timeline.

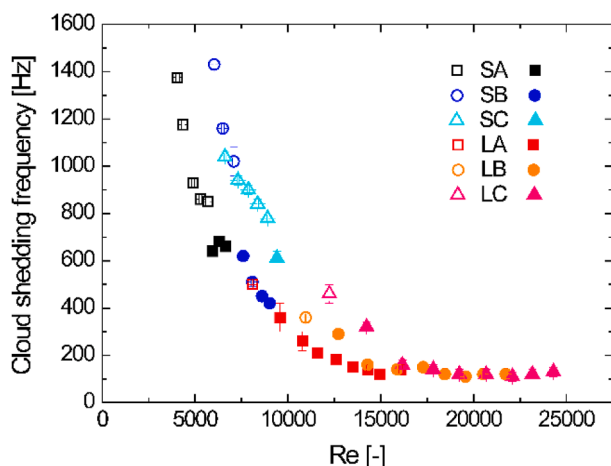


**Fig. 7.** Cloud shedding frequency at different Reynolds numbers in the six channel geometries. The full symbols represent the full cavitation cloud shedding regimes, while the empty symbols show the developed cavitation regimes with partial or transitory cloud shedding.

shedding process in the large channel series, taken over 50ms (at 100kFPS), corresponding to at least 5 cloud shedding events per channel at a specific driving pressure condition. The white areas show the area and the path of the cavitation cloud in each channel; while the weak streak shows the path of residual bubble runoff, following the collapse. We can clearly see the LA channel's linear progression of the average cloud path, while for the other two channels there is a sharp variation to the linear advance at 5 and 6 bar, for LC and LB respectively. This corresponds to the end of the divergent part of the micro venturi, where the sharp increase in the channel cross-section will tend to induce the cavitation cloud collapse for any vapor structures that reach this region. Fig. 9 shows the cavitation cloud length at different driving pressures, with the dashed line indicating the approximated end of the divergent part of the channel. The evolution of the average cloud length can be observed, as the slopes at or after the dashed line are significantly

diminished.

## 4. Discussion

### 4.1. Microchannel radical production

The existence of distinct metastable behavior in smaller channels, shown in Fig. 2a, indicates that the smooth surfaces of the laser cut stainless steel sheets and the plexiglass walls, as well as the filtration of the liquid, do not contribute to the nucleation and help water retain its tensile strength, demonstrated by the resistance to the phase transition. This also manifests itself as a difference between cavitation inception and desinence, which is often reported in publications studying microscale HC (Ayela et al., 2017, 2013; Medrano et al., 2012, 2011). We can see this behavior clearly in our small channel series, and to a lesser extent on the larger channel as well. In Fig. 2a, mass flow curves at different driving pressures show the flow hysteresis for metastable small channel group; the empty symbols represent the single-phase flow and the full symbol cavitating flow. The ROS production of the channels either at higher mass flow or driving pressure seems to increase. Furthermore, the ROS production also increases with the increasing hydraulic diameter of the channel. However, when the ROS production per treated liquid volume is considered, the biggest channels are not the most efficient. In this respect, the LA channel showed the best production in the study, and SA and SB performing best for the small series group. The latter two also approach the amol/ml values of the largest channel tested in the series – LC. In fact, the lowest amol/ml yield in each channel group was shown from the widest channels (SC and LC), indicating that this aspect ratio is not a geometric optimum. Moreover, it serves as an example of how this method facilitates optimization of flow and geometric parameters, while providing a rapid and non-intrusive ROS production readout, as well as allowing for a more in-depth analysis of the chemical production. In Fig. 3a, when considering the ROS production at varying hydraulic power of the flow, we can observe similar linear trends appearing for all channels, with the exception of channel SC, which shows a lower slope (k-value) to other channels. Again, the least productive channels in each group seem to be the widest aspect ratio channels (SC and LC), as we can see other channels producing higher ROS yields at a comparable hydraulic power value. Fig. 3b, considers the amol/ml with dimensionless numbers, used to evaluate the cavitation intensity ( $\sigma$  and  $\sigma_{cav}/\sigma$ ). Rating the intensity of the cavitation process is generally difficult, as depending on the phenomenon studied, different parameters of the individual bubble and higher structures dynamics as well as physical parameters will be at play (Sarc et al., 2017). The high speeds involved in our micro channels produce low  $\sigma$ , indicating intense cavitation compared to macroscale numbers. Our data shows that when plotting the amol/ml as a function of  $\sigma$ , the two channel height groups also form two distinct groups, producing similar amol/ml values at similar flow conditions. However, more interestingly, when scaling the  $\sigma$  value with its value at cavitation inception ( $\sigma_{cav}/\sigma$ ), the channels seem to adopt a unified linear progression, with the exception of SB channel, where the amol/ml rate raises faster. This could potentially be due to the fine geometry of the surface roughness at the constriction of the SB channel, which can influence the measured  $p_{cav}$  value for that particular channel, as it seems to be somewhat higher than the SA and SC channels. In Fig. 3c, the ROS yield per processed flow is examined at different  $Q-Q_{cav}$  values. The small-scale channels SA and SB amol/ml production mostly overlaps, while this no longer holds for the SC channel and even less so for the large group channels, whose k-values gradually decrease with increasing channel cross-section. Interestingly, the two smallest channels show the same linear trend observed in literature for a comparable cross-section micro-diaphragm channels ( $D_h = 0.125\text{mm}$  and the  $k \approx 74,7$  amol/ml) (Podbevšek et al., 2021a). This indicates that a common fundamental mechanism, linked to the flow at the microscale, could be governing the radical production, which lessens in relevance with increasing channel size.

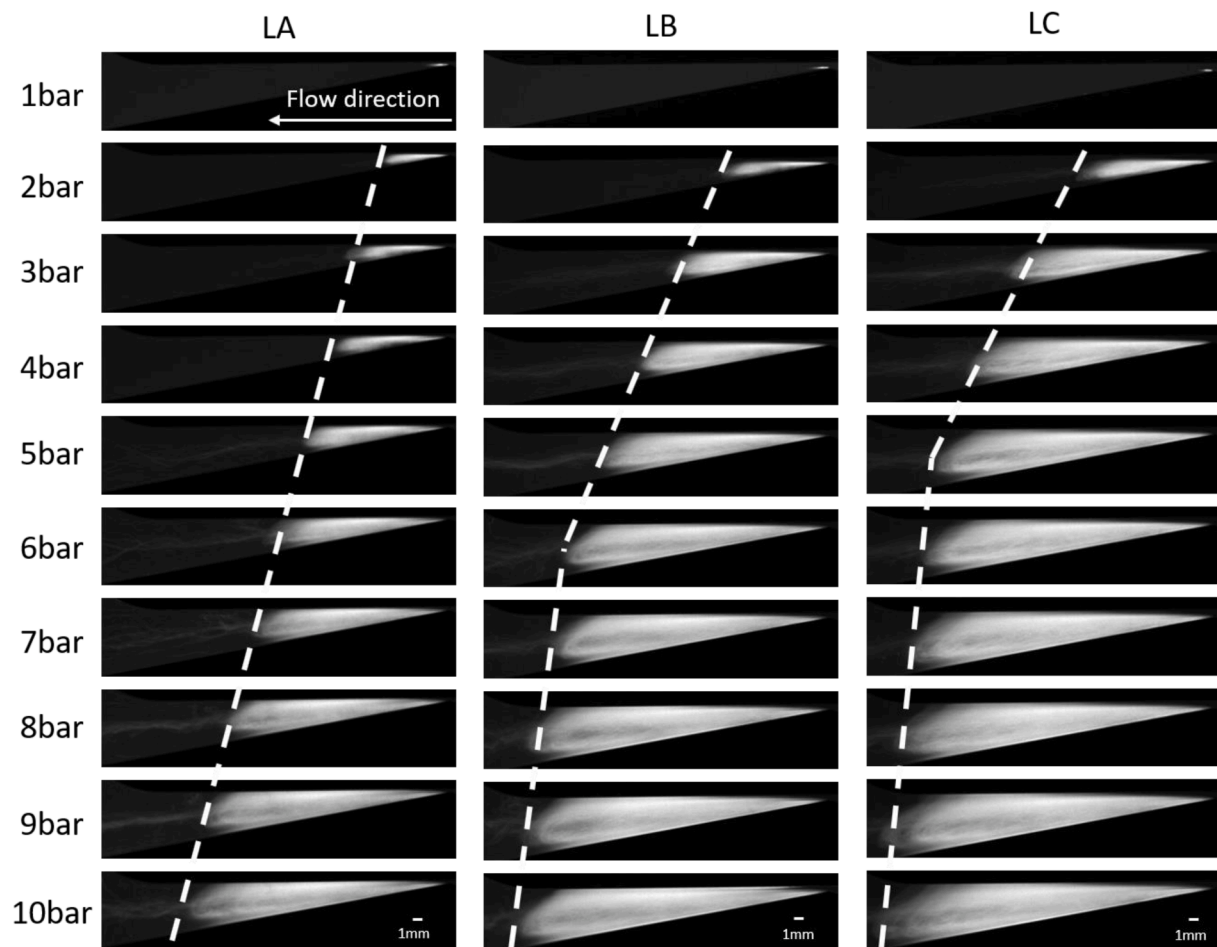


**Fig. 8.** Standard deviations analysis over 5000 consecutive images (50ms) or >5 cloud shedding events, showing the cloud shedding process in the large channel series ( $H = 450\mu\text{m}$ ). The images show the typical average cloud path - L, that the cloud makes throughout its growth process in the diverging part of the micro-channel. The less intense white trail leading off the cavity length is the path of the residual bubbles. The flow direction is flow right to left.

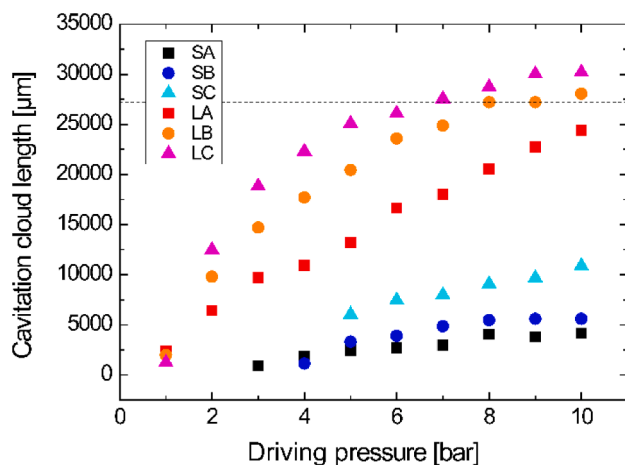


**Fig. 9.** The evolution of the average cavity length with driving pressure, with the dashed line representing the length of the divergent part of the downstream channels.

#### 4.2. Time resolved oxidation dynamics and the underlying cavitation structure

As the radical production mechanism for cavitation is linked to the thermodynamic extremes at peak bubble collapse, it is inevitable that

any study on the chemical yield from hydrodynamic cavitation will have to consider the dynamics of the vaporous structures in the channel. The simultaneous collapse of individual bubbles, making up the cavitation cloud, is a powerful and dominant structure dynamics event and it is natural to assume that the radical production could be predominantly linked to its implosion. However, our results point to the contrary, as the photon arrival times are randomly distributed in the periods when the cavitation stream is present, and therefore not linked to the cloud shedding frequency. In Fig. 6, we can see the overlap of the photon arrival times and the cavitation stream presence, obtained from image analysis. It is important to stress that the chemiluminescence activity can only be recorded in blackout conditions, therefore the two data sets cannot be acquired simultaneously, however they do represent the typical periodical activity for the channels at the particular flow conditions. From the figure it is clear that the photon arrival times follow the presence of the cavitation stream, not a singular event like a cloud collapse. A burst-like generation of radicals, as expected from a cavitation cloud collapse, should yield an exponential decay type distribution of the photon arrival times in periodic sequences, corresponding to the cavitation cloud shedding frequencies. However, what we observe is the CL reactions randomly distributed in time, when the cavitation stream is present and periods of chemiluminescence inactivity during the periodic retreat of the stream. Notably, we see the photon arrival gap and period match very well with the gap and period in the high-speed recordings, showing that the CL reactions are not taking place when the cavitation stream disappears from the flow. This is strong evidence that the individual bubble collapses in the cavitation stream are in fact responsible

for the ROS production. Furthermore, the radical production from cavitation cloud collapse would be correlated to the cloud shedding frequency, which is not the case for our channels. In Fig. 7, we see higher cloud shedding frequencies at lower driving pressure (lower Re values), while the radical production for all channels rises linearly with increasing flow conditions. We can also see that there is a transition from developed (empty symbol) to full (filled symbol) cavitation cloud shedding regime in the flow, more clearly pronounced in the small channel series. The small channel group tends to form distinctive cavitation clouds when the frequency approaches 600Hz, while for the large channel group the value is around 300Hz. Above those frequencies, the cloud will not fully form and will often just manifest as a cavitation stream burst. For example, SC channel only shows full cavitation shedding in the last (10bar) measured point, yet this transition is not observed as a deviation from the linear ROS production trends. In Fig. 8 as well as Fig. 9, the cavitation cloud evolution is shown limited by the channel design for the largest two channels, yet this effect does not seem to affect the ROS production. We see that in channels LB and LC, as the cavitation cloud path advance becomes limited, the ROS/ml rates continue their linear trend, as observed with other parameters. This suggests that the radical production does not seem to be directly correlated to the void fraction, represented by the average cloud presence in the channel, as suggested in previous publications on micro-diaphragm channels (Podbevšek et al., 2018). It is most likely that the ROS production is linked to the intensity or the relative time of the cavitation stream presence in the channel, rather than simply the void fraction.

## 5. Conclusions

A study on the radical production for hydrodynamic cavitation was conducted at the micro to the milli scale transition in venturi microchannels via luminol chemiluminescent reactions. A general trend of increasing chemical yield was observed with increasing hydraulic diameter of the channel and with increasing driving pressure. However, in both channel series it was observed that when considering the chemical yield per treated volume of liquid, the biggest channels did not always produce more, indicating that an optimal geometry exists for the given flow parameters. Similar trendlines were observed between the channels of vastly different cross-section, when observed at different hydraulic power and other normalized cavitation parameters. For the latter parameters, the chemical production per processed volume for the smallest two microchannels seem to overlap, as well as being in line with observations in literature for similar sized microdiaphragm channels. Furthermore, this study also sheds light on the bubble dynamics mechanisms relevant at the microscale hydrodynamic cavitation. The photon arrival time analysis shows that the cavitation cloud collapse is not responsible for the radicals produced in the two-phase flow. This is corroborated by the lack of correlation between the cloud shedding frequency and the radical yield. Instead, the cavitation bubble stream made up of individual smaller bubbles growing and collapsing, was shown to be responsible for the chemical effects of the micro/milli scale hydrodynamic cavitation, indicating it could also be the dominant mechanism at the macroscale.

## Declaration of Competing Interest

The authors declare that they have no known competing financial interests or personal relationships that could have appeared to influence the work reported in this paper.

## Acknowledgment

The authors thank the NanOpTec Center (Lyon, France) for access to the optical facilities. The authors acknowledge the financial support from the European Research Council (ERC) under the European Union's Framework Program for research and innovation, Horizon 2020 (grant

agreement n° 771567 — CABUM) and the Slovenian Research Agency (research projects No. J2-3057, L7-3184, J7-2601 and research core funding No. P2-0422).

## References

- Aghdam, A.S., Ghorbani, M., Deprem, G., Cebeci, F.Ç., Koşar, A., 2019. A New Method for Intense Cavitation Bubble Generation on Layer-by-Layer Assembled SLIPS. *Sci. Rep.* 9, 1–13. <https://doi.org/10.1038/s41598-019-48175-4>.
- Arrojo, S., Benito, Y., 2008. A theoretical study of hydrodynamic cavitation. *Ultrason. Sonochem.* 15, 203–211. <https://doi.org/10.1016/j.ultsonch.2007.03.007>.
- Arrojo, S., Nerín, C., Benito, Y., 2007. Application of salicylic acid dosimetry to evaluate hydrodynamic cavitation as an advanced oxidation process. *Ultrason. Sonochem.* 14, 343–349. <https://doi.org/10.1016/j.ultsonch.2006.06.007>.
- Ayela, F., Cherief, W., Colombet, D., Ledoux, G., Martini, M., Mossaz, S., Podbevšek, D., Qiu, X., Tillement, O., 2017. Hydrodynamic Cavitation through “Labs on a Chip”: From Fundamentals to Applications. *Oil Gas Sci. Technol. – Rev. D'IFP Energ. Nouv.* 72, 19. <https://doi.org/10.2516/ogst/2017010>.
- Ayela, F., Medrano-Muñoz, M., Amans, D., Dujardin, C., Brichart, T., Martini, M., Tillement, O., Ledoux, G., 2013. Experimental evidence of temperature gradients in cavitating microflows seeded with thermosensitive nanopropes. *Phys. Rev. E Stat. Nonlin. Soft Matter Phys.* 88, 043016. <https://doi.org/10.1103/PhysRevE.88.043016>.
- Batoeva, A.A., Aseev, D.G., Sizykh, M.R., Vol'nov, I.N., 2011. A study of hydrodynamic cavitation generated by low pressure jet devices. *Russ. J. Appl. Chem.* 84, 1366. <https://doi.org/10.1134/S107042721108012X>.
- Braeutigam, P., Wu, Z.-L., Stark, A., Ondruschka, B., 2009. Degradation of BTEX in Aqueous Solution by Hydrodynamic Cavitation. *Chem. Eng. Technol.* 32, 745–753. <https://doi.org/10.1002/ceat.200800626>.
- Cako, E., Darvishi Cheshmeh Soltani, R., Sun, X., Boczkaj, G., 2022. Desulfurization of raw naphtha cuts using hybrid systems based on acoustic cavitation and advanced oxidation processes (AOPs). *Chem. Eng. J.* 439, 135354. <https://doi.org/10.1016/j.cej.2022.135354>.
- Cole, G.S., Scaringe, R.P., Roth, R.P., Peles, Y., 2006. System Evaluation of Cavitation Enhanced Heat Transfer in Microchannels (SAE Technical Paper No. 2006-01-3062). SAE International, Warrendale, PA. <https://doi.org/10.4271/2006-01-3062>.
- Dular, M., Bachert, B., Stoffel, B., Širok, B., 2004. Relationship between cavitation structures and cavitation damage. *Wear* 257, 1176–1184. <https://doi.org/10.1016/j.wear.2004.08.004>.
- Dular, M., Stoffel, B., Širok, B., 2006. Development of a cavitation erosion model. *Wear* 261, 642–655. <https://doi.org/10.1016/j.wear.2006.01.020>.
- Fedorov, K., Dinesh, K., Sun, X., Darvishi Cheshmeh Soltani, R., Wang, Z., Sonawane, S., Boczkaj, G., 2022. Synergistic effects of hybrid advanced oxidation processes (AOPs) based on hydrodynamic cavitation phenomenon – A review. *Chem. Eng. J.* 432, 134191. <https://doi.org/10.1016/j.cej.2021.134191>.
- Fedorov, K., Plata-Gryl, M., Khan, J.A., Boczkaj, G., 2020. Ultrasound-assisted heterogeneous activation of persulfate and peroxydisulfate by asphaltenes for the degradation of BTEX in water. *J. Hazard. Mater.* 397, 122804. <https://doi.org/10.1016/j.jhazmat.2020.122804>.
- Fedorov, K., Sun, X., Boczkaj, G., 2021. Combination of hydrodynamic cavitation and SR-AOPs for simultaneous degradation of BTEX in water. *Chem. Eng. J.* 417, 128081. <https://doi.org/10.1016/j.cej.2020.128081>.
- Fernandez Rivas, D., Ashokkumar, M., Leong, T., Yasui, K., Tuziuti, T., Kentish, S., Lohse, D., Gardeniers, H.J.G.E., 2012. Sonoluminescence and sonochemiluminescence from a microreactor. *Ultrason. Sonochem.* 19, 1252–1259. <https://doi.org/10.1016/j.ultsonch.2012.04.008>.
- Gągól, M., Cako, E., Fedorov, K., Soltani, R.D.C., Przyjazny, A., Boczkaj, G., 2020. Hydrodynamic cavitation based advanced oxidation processes: Studies on specific effects of inorganic acids on the degradation effectiveness of organic pollutants. *J. Mol. Liq.* 307, 113002. <https://doi.org/10.1016/j.molliq.2020.113002>.
- Gągól, M., Przyjazny, A., Boczkaj, G., 2018. Wastewater treatment by means of advanced oxidation processes based on cavitation – A Review. *Chem. Eng. J.* 338. <https://doi.org/10.1016/j.cej.2018.01.049>.
- Gevari, M.T., Ghorbani, M., Svagan, A.J., Grishenkov, D., Kosar, A., 2019. Energy harvesting with micro scale hydrodynamic cavitation-thermoelectric generation coupling. *AIP Adv* 9, 105012. <https://doi.org/10.1063/1.5115336>.
- Ghorbani, M., 2021. The Hydrodynamic Cavitation Manifestation in Small Chips. *IEEE Access* 9, 110517–110524. <https://doi.org/10.1109/ACCESS.2021.3102898>.
- Ghorbani, M., Chen, H., Villanueva, L.G., Grishenkov, D., Koşar, A., 2018a. Intensifying cavitating flows in microfluidic devices with poly(vinyl alcohol) (PVA) microbubbles. *Phys. Fluids* 30, 102001. <https://doi.org/10.1063/1.5051606>.
- Ghorbani, M., Mohammadi, A., Motezakker, A.R., Villanueva, L.G., Leblebici, Y., Koşar, A., 2017a. Energy Harvesting in Microscale with Cavitating Flows. *ACS Omega* 2, 6870–6877. <https://doi.org/10.1021/acsomega.7b01204>.
- Ghorbani, M., Sadaghiani, A.K., Villanueva, L.G., Koşar, A., 2018b. Hydrodynamic cavitation in microfluidic devices with roughened surfaces. *J. Micromechanics Microengineering* 28, 075016. <https://doi.org/10.1088/1361-6439/aab9d0>.
- Ghorbani, M., Sadaghiani, A.K., Yidiz, M., Koşar, A., 2017b. Experimental and numerical investigations on spray structure under the effect of cavitation phenomenon in a microchannel. *J. Mech. Sci. Technol.* 31, 235–247. <https://doi.org/10.1007/s12206-016-1226-y>.

- Ghorbani, M., Sozer, C., Alcan, G., Unel, M., Ekici, S., Uvet, H., Koşar, A., 2018c. Biomedical device prototype based on small scale hydrodynamic cavitation. *AIP Adv* 8, 035108. <https://doi.org/10.1063/1.5005048>.
- Gielen, B., Marchal, S., Jordens, J., Thomassen, L.C.J., Braeken, L., Van Gerven, T., 2016. Influence of dissolved gases on sonochemistry and sonoluminescence in a flow reactor. *Ultrason. Sonochem.* 31, 463–472. <https://doi.org/10.1016/j.ultronch.2016.02.001>.
- Gogate, P.R., Shirgaonkar, I.Z., Sivakumar, M., Senthilkumar, P., Vichare, N.P., Pandit, A.B., 2001. Cavitation reactors: Efficiency assessment using a model reaction. *AIChE J* 47, 2526–2538. <https://doi.org/10.1002/aic.690471115>.
- Gothsch, T., Schilcher, C., Richter, C., Beinert, S., Dietzel, A., Büttgenbach, S., Kwade, A., 2015. High-pressure microfluidic systems (HPMS): flow and cavitation measurements in supported silicon microsystems. *Microfluid. Nanofluidics* 18, 121–130. <https://doi.org/10.1007/s10404-014-1419-6>.
- Guittonneau, F., Abdelouas, A., Grambow, B., Huclier, S., 2010. The effect of high power ultrasound on an aqueous suspension of graphite. *Ultrason. Sonochem.* 17, 391–398. <https://doi.org/10.1016/j.ultronch.2009.08.011>.
- Hatanaka, S.-I., Mitome, H., Yasui, K., Hayashi, S., 2002. Single-bubble sonochemiluminescence in aqueous luminol solutions. *J. Am. Chem. Soc.* 124, 10250–10251.
- Hosseinpour Shafaghi, A., Rokhsar Talabazar, F., Zuvín, M., Talebian Gevari, M., Villanueva, L.G., Ghorbani, M., Koşar, A., 2021. On cavitation inception and cavitating flow patterns in a multi-orifice microfluidic device with a functional surface. *Phys. Fluids* 33, 032005. <https://doi.org/10.1063/1.50037736>.
- Kalumuck, K.M., Chahine, G.L., 2000. The Use of Cavitating Jets to Oxidize Organic Compounds in Water. *J. Fluids Eng.* 122, 465–470. <https://doi.org/10.1115/1.1286993>.
- Kim, J., Michelin, S., Hilbers, M., Martinelli, L., Chaudan, E., Amselem, G., Fradet, E., Boillot, J.-P., Brouwer, A.M., Baroud, C.N., Peretti, J., Gacoin, T., 2017. Monitoring the orientation of rare-earth-doped nanorods for flow shear tomography. *Nat. Nanotechnol.* 12, 914–919. <https://doi.org/10.1038/nnano.2017.111>.
- Lalwani, J., Gupta, A., Thatikonda, S., Subrahmanyam, C., 2020. Oxidative treatment of crude pharmaceutical industry effluent by hydrodynamic cavitation. *J. Environ. Chem. Eng.* 8, 104281. <https://doi.org/10.1016/j.jece.2020.104281>.
- Lee, J., Seliger, H.H., 1972. Quantum Yields of the Luminol Chemiluminescence Reaction in Aqueous and Aprotic Solvents\*. *Photochem. Photobiol.* 15, 227–237. <https://doi.org/10.1111/j.1751-1097.1972.tb06241.x>.
- McMurray, H.N., Wilson, B.P., 1999. Mechanistic and Spatial Study of Ultrasonically Induced Luminol Chemiluminescence. *J. Phys. Chem. A* 103, 3955–3962. <https://doi.org/10.1021/jp984503r>.
- Medrano, M., Pellone, C., Zermatten, P.J., Ayela, F., 2012. Hydrodynamic cavitation in microsystems. II. Simulations and optical observations. *Phys. Fluids* 24, 047101. <https://doi.org/10.1063/1.3699067>.
- Medrano, M., Zermatten, P.J., Pellone, C., Franc, J.P., Ayela, F., 2011. Hydrodynamic cavitation in microsystems. I. Experiments with deionized water and nanofluids. *Phys. Fluids* 23, 127103. <https://doi.org/10.1063/1.3671682>.
- Mishra, Chandan, Peles, Y., 2006. An experimental investigation of hydrodynamic cavitation in micro-Venturis. *Phys. Fluids* 18, 103603. <https://doi.org/10.1063/1.2360996>.
- Mishra, C., Peles, Y., 2006. Development of Cavitation in Refrigerant (R-123) Flow Inside Rudimentary Microfluidic Systems. *J. Microelectromechanical Syst.* 15, 1319–1329. <https://doi.org/10.1109/JMEMS.2006.872230>.
- Mishra, Chandan, Peles, Y., 2005a. Flow visualization of cavitating flows through a rectangular slot micro-orifice ingrained in a microchannel. *Phys. Fluids* 17, 113602. <https://doi.org/10.1063/1.2132289>.
- Mishra, C., Peles, Y., 2005. Size scale effects on cavitating flows through microorifices entrenched in rectangular microchannels. *J. Microelectromechanical Syst.* 14, 987–999. <https://doi.org/10.1109/JMEMS.2005.851800>.
- Mishra, Chandan, Peles, Y., 2005b. Hydrodynamic Cavitation in Flow Through Micro-Constriction Elements Entrenched in Rectangular Microchannels 761–770. <https://doi.org/10.1115/FEDSM2005-77406>.
- Mishra, C., Peles, Y., 2004. Cavitation in flow through a micro-orifice inside a silicon microchannel. *Phys. Fluids* 17, 013601. <https://doi.org/10.1063/1.1827602>.
- Mishra, K.P., Gogate, P.R., 2010. Intensification of degradation of Rhodamine B using hydrodynamic cavitation in the presence of additives. *Sep. Purif. Technol.* 75, 385–391. <https://doi.org/10.1016/j.seppur.2010.09.008>.
- Morison, K.R., Hutchinson, C.A., 2009. Limitations of the Weissler reaction as a model reaction for measuring the efficiency of hydrodynamic cavitation. *Ultrason. Sonochem.* 16, 176–183. <https://doi.org/10.1016/j.ultronch.2008.07.001>.
- Mossaz, S., Colombet, D., Ayela, F., 2017. Hydrodynamic cavitation of binary liquid mixtures in laminar and turbulent flow regimes. *Exp. Therm. Fluid Sci.* 80, 337–347. <https://doi.org/10.1016/j.exptthermfluidsci.2016.08.001>.
- Nayebzadeh, A., Wang, Y., Tabkhi, H., Shin, J.-H., Peles, Y., 2018. Cavitation behind a circular micro pillar. *Int. J. Multiph. Flow* 98, 67–78. <https://doi.org/10.1016/j.ijmultiphaseflow.2017.08.012>.
- Peles, Y., 2008. Cavitation in Microdomains, in: Prof, D.L. (Ed.), *Encyclopedia of Microfluidics and Nanofluidics*. Springer US, pp. 197–201. [https://doi.org/10.1007/978-0-387-48998-8\\_170](https://doi.org/10.1007/978-0-387-48998-8_170).
- Peles, Y., Schneider, B., 2006. Hydrodynamic Cavitation and Boiling in Refrigerant (R-123) Flow Inside Microchannels 1323–1332. <https://doi.org/10.1115/ICNMM2006-96030>.
- Perrin, L., Colombet, D., Ayela, F., 2021. Comparative study of luminescence and chemiluminescence in hydrodynamic cavitating flows and quantitative determination of hydroxyl radicals production. *Ultrason. Sonochem.* 70, 105277. <https://doi.org/10.1016/j.ultronch.2020.105277>.
- Podbešek, D., Colombet, D., Ayela, F., Ledoux, G., 2021a. Localization and quantification of radical production in cavitating flows with luminol chemiluminescent reactions. *Ultrason. Sonochem.* 71, 105370. <https://doi.org/10.1016/j.ultronch.2020.105370>.
- Podbešek, D., Colombet, D., Ledoux, G., Ayela, F., 2018. Observation of chemiluminescence induced by hydrodynamic cavitation in microchannels. *Ultrason. Sonochem.* 43, 175–183. <https://doi.org/10.1016/j.ultronch.2018.01.004>.
- Podbešek, D., Petkovšek, M., Ohl, C.D., Dular, M., 2021b. Kelvin-Helmholtz Instability Governs the Cavitation Cloud Shedding in Venturi Microchannel. *Int. J. Multiph. Flow* 103700. <https://doi.org/10.1016/j.ijmultiphaseflow.2021.103700>.
- Price, G.J., Harris, N.K., Stewart, A.J., 2010. Direct observation of cavitation fields at 23 and 515kHz. *Ultrason. Sonochem.* 17, 30–33. <https://doi.org/10.1016/j.ultronch.2009.04.009>.
- Qiu, X., Bouchiat, V., Colombet, D., Ayela, F., 2019. Liquid-phase exfoliation of graphite into graphene nanosheets in a hydrocavitating ‘lab-on-a-chip’. *RSC Adv* 9, 3232–3238. <https://doi.org/10.1039/C8RA05976D>.
- Qiu, X., Cherief, W., Colombet, D., Ayela, F., 2017. A simple process to achieve microchannels geometries able to produce hydrodynamic cavitation. *J. Micromechanics Microengineering* 27, 047001. <https://doi.org/10.1088/1361-6439/aa5fa5>.
- Rayaroth, M.P., Aravindakumar, C.T., Shah, N.S., Boczkaj, G., 2022. Advanced oxidation processes (AOPs) based wastewater treatment - unexpected nitration side reactions - a serious environmental issue: A review. *Chem. Eng. J.* 430, 133002. <https://doi.org/10.1016/j.cej.2021.133002>.
- Renaudin, V., Gondrexon, N., Boldo, P., Pétrier, C., Bernis, A., Gonthier, Y., 1994. Method for determining the chemically active zones in a high-frequency ultrasonic reactor. *Ultrason. Sonochem.* 1, S81–S85. [https://doi.org/10.1016/1350-4177\(94\)90002-7](https://doi.org/10.1016/1350-4177(94)90002-7).
- Rokhsar Talabazar, F., Jafarpour, M., Zuvín, M., Chen, H., Gevari, M.T., Villanueva, L.G., Grishenkov, D., Koşar, A., Ghorbani, M., 2021. Design and fabrication of a vigorous ‘cavitation-on-a-chip’ device with a multiple microchannel configuration. *Microsyst. Nanoeng.* 7, 1–13. <https://doi.org/10.1038/s41378-021-00270-1>.
- Rooze, J., André, M., van der Gulik, G.-J.S., Fernández-Rivas, D., Gardeniens, J.G.E., Rebrov, E.V., Schouten, J.C., Keurentjes, J.T.F., 2012. Hydrodynamic cavitation in micro channels with channel sizes of 100 and 750 micrometers. *Microfluid. Nanofluidics* 12, 499–508. <https://doi.org/10.1007/s10404-011-0891-5>.
- Rooze, J., Rebrov, E.V., Schouten, J.C., Keurentjes, J.T.F., 2013. Dissolved gas and ultrasonic cavitation - A review. *Ultrason. Sonochem.* 20, 1–11. <https://doi.org/10.1016/j.ultronch.2012.04.013>.
- Šarc, A., Stepišnik-Perdih, T., Petkovšek, M., Dular, M., 2017. The issue of cavitation number value in studies of water treatment by hydrodynamic cavitation. *Ultrason. Sonochem.* 34, 51–59. <https://doi.org/10.1016/j.ultronch.2016.05.020>.
- Schlender, M., Minke, K., Schuchmann, H.P., 2016. Sono-chemiluminescence (SCL) in a high-pressure double stage homogenization processes. *Chem. Eng. Sci.* 142, 1–11. <https://doi.org/10.1016/j.ces.2015.11.028>.
- Schneider, B., Koşar, A., Peles, Y., 2007. Hydrodynamic cavitation and boiling in refrigerant (R-123) flow inside microchannels. *Int. J. Heat Mass Transf.* 50, 2838–2854. <https://doi.org/10.1016/j.ijheatmasstransfer.2007.01.002>.
- Singh, R., Peles, Y., 2009. The effects of fluid properties on cavitation in a micro domain. *J. Micromechanics Microengineering* 19, 025009. <https://doi.org/10.1088/0960-1317/19/2/025009>.
- Son, Y., No, Y., Kim, J., 2020. Geometric and operational optimization of 20-kHz probe-type sonoreactor for enhancing sonochemical activity. *Ultrason. Sonochem.* 65, 105065. <https://doi.org/10.1016/j.ultronch.2020.105065>.
- Stieger, T., Agha, H., Schoen, M., Mazza, M.G., Sengupta, A., 2017. Hydrodynamic cavitation in Stokes flow of anisotropic fluids. *Nat. Commun.* 8, 15550. <https://doi.org/10.1038/ncomms15550>.
- Suslick, K.S., 1997. Sonoluminescence and sonochemistry. *Proc. IEEE Ultrason. Symp.* 1, 523–532.
- Suslick, K.S., 1989. The Chemical Effects of Ultrasound. *Sci. Am.* 260, 80–86. <https://doi.org/10.1038/scientificamerican0289-80>.
- Wang, X., Wang, J., Guo, P., Guo, W., Wang, C., 2009. Degradation of rhodamine B in aqueous solution by using swirling jet-induced cavitation combined with H<sub>2</sub>O<sub>2</sub>. *J. Hazard. Mater.* 169, 486–491. <https://doi.org/10.1016/j.jhazmat.2009.03.122>.
- Wood, R.J., Lee, J., Bussemaker, M.J., 2017. A parametric review of sonochemistry: Control and augmentation of sonochemical activity in aqueous solutions. *Ultrason. Sonochem.* 38, 351–370. <https://doi.org/10.1016/j.ultronch.2017.03.030>.
- Yin, H., Qiao, Y., Cao, H., Li, Z., Wan, M., 2014. Cavitation mapping by sonochemiluminescence with less bubble displacement induced by acoustic radiation force in a 1.2MHz HIFU. *Ultrason. Sonochem.* 21, 559–565. <https://doi.org/10.1016/j.ultronch.2013.10.005>.
- Zupanc, M., Pandur, Ž., Stepišnik Perdih, T., Stopar, D., Petkovšek, M., Dular, M., 2019. Effects of cavitation on different microorganisms: The current understanding of the mechanisms taking place behind the phenomenon. A review and proposals for further research. *Ultrason. Sonochem.* 57, 147–165. <https://doi.org/10.1016/j.ultronch.2019.05.009>.
- Zupanc, M., Petkovšek, M., Zevnik, J., Kozmus, G., Šmid, A., Dular, M., 2020. Anomalies detected during hydrodynamic cavitation when using salicylic acid dosimetry to measure radical production. *Chem. Eng. J.* 396, 125389. <https://doi.org/10.1016/j.cej.2020.125389>.